# Forced deterministic dynamics on a random energy landscape: Implications for the physics of amorphous solids

Asaf Szulc [1], Omri Gat [2] and Ido Regev [3,*]

[1]*Department of Physics, Ben Gurion University of the Negev, Beer Sheva 84105, Israel*
[2]*Racah Institute of Physics, The Hebrew University of Jerusalem, Jerusalem 91904, Israel*
[3]*The Jacob Blaustein Institutes for Desert Research, Ben-Gurion University of the Negev, Sede Boqer Campus 84990, Israel*

(Received 6 January 2020; accepted 21 April 2020; published 27 May 2020)

The dynamics of supercooled liquids and plastically deformed amorphous solids is known to be dominated by the structure of their rough energy landscapes. Recent experiments and simulations on amorphous solids subjected to oscillatory shear at athermal conditions have shown that for small strain amplitudes these systems reach limit cycles of different periodicities after a transient. However, for larger strain amplitudes the transients become longer and for strain amplitudes exceeding a critical value the system reaches a diffusive steady state. This behavior cannot be explained using the current mean-field models of amorphous plasticity. Here we show that this phenomenology can be described and explained using a simple model of forced dynamics on a multidimensional random energy landscape. In this model, the existence of limit cycles can be ascribed to confinement of the dynamics to a small part of the energy landscape which leads to self-intersection of state-space trajectories and the transition to the diffusive regime for larger forcing amplitudes occurs when the forcing overcomes this confinement.

DOI: 10.1103/PhysRevE.101.052616

## I. INTRODUCTION

Random energy landscapes are an ubiquitous feature of disordered systems such as spin-glasses and structural glasses [1,2]. One can think of the dynamics of a fluid as the diffusion of a point particle on a random energy landscape embedded in a space of dimensionality equal to the number of particles times the number of space dimensions [3]. At high temperatures, the dynamics is dominated by transitions between saddles, which do not require thermal activation [4], whereas in a supercooled liquid, or a liquid which is close to the glass transition, the dynamics is thermally activated; it is dominated by energy barriers which determine the rate of relaxation [5,6]. At even lower temperatures when the system is in a glassy state, it spends most of the time close to potential energy minima [7]. This premise has led to increased interest in understanding the structure of such high-dimensional landscapes with emphasis on characterizing the density of minima and saddle points under different conditions [8–15]. Specifically, recent studies have shown that Gaussian landscapes and $p$-spin glasses undergo a geometrical phase transition from having an exponentially large number of minima to having one minimum when an external potential is varied at zero temperature [9,11,15]. When an amorphous solid is subjected to an externally applied shear, minima become destabilized, thus causing the system to move from one minimum to the other, exploring different configurations which correspond to different points on the energy landscape [16]. Theoretical approaches based on describing the dynamics of amorphous solids in terms of a zero- or one-dimensional energy landscape have been highly successful [17,18]. However, recent experiments and simulations studying the response of amorphous and granular materials [19–33], as well as other random systems [34–37], to oscillatory shear of varying amplitudes under quasistatic, athermal conditions, have revealed interesting phenomena which cannot be explained using a zero- or one-dimensional energy landscape [26,38–40]. The typical response for small driving amplitudes is transient random dynamics that ends up in a limit cycle of a period that is an integer multiple of the driving period (this is possible since at zero temperature the dynamics is deterministic). For large driving amplitudes, the system typically reaches a nonrepetitive, diffusive, steady state [20–30]. Since one-dimensional dynamical systems are topologically restricted, they will always reach a limit cycle when subjected to oscillatory forcing. However, as we show in the following, in a multidimensional energy landscape we observe a transition from periodic to diffusive behavior in accordance with the observations from molecular dynamics simulations and experiments.

The energy function $\mathcal{U}$ of a typical material (fluid or solid) is a scalar function of the vector of coordinates which can be thought of as a surface in the $Nd$-dimensional configuration space:

$$\mathcal{U}(\boldsymbol{r}_1, \boldsymbol{r}_2, \ldots, \boldsymbol{r}_N) = \sum_{i \neq j}^{N} u_{ij}(|\boldsymbol{r}_i - \boldsymbol{r}_j|), \tag{1}$$

where $N$ is the number of particles, $\boldsymbol{r}_i$ are the position vectors of the different particles, and $u_{ij}(x)$ is a two-body interaction. Under athermal conditions, the dynamics of a periodically forced amorphous solid is equivalent to the dynamics of a particle moving on a rugged surface embedded in a space with

*regevid@bgu.ac.il

 

dimensionality equal to that of the configuration space and subjected to a periodic external force. For an amorphous solid made of $N$ particles, the dimensionality of the configuration space is $3N$ ($2N$ for a two-dimensional system of particles). $N$ in molecular dynamics simulations varies between $N = 1000$ and $N = 64\,000$ or more, which means that the configuration-space dimensionality is typically at least $2N = 2000$. Since most configurations in a liquid or an amorphous solid are disordered, the energy function has a large number of minima, maxima and saddles, distributed randomly in configuration space. For this reason the energy function is called "the energy landscape" of the system. Recently, Refs. [22,38], one of us suggested that, at least in some models of amorphous solids, the phenomenology of transient dynamics, limit cycles of different periodicities, and a crossover into diffusive dynamics can be explained in terms of a multidimensional energy landscape. Here we use a specialized algorithm to study deterministic dynamics on a random energy landscape in relatively large space dimensions. We show that this model can reproduce some of the dynamics observed in amorphous solids cyclicly sheared at low temperatures, such as limit cycles of varying periodicities and a transition from repetitive to diffusive dynamics. We explain how this behavior emerges naturally from the interplay between the randomness of the landscape, the periodicity of the forcing, and the deterministic nature of the dynamics. Finally, we discuss how the ability to reproduce the dynamics observed in amorphous solids using a Gaussian landscape model can lead to a better understanding of the irreversibility transition.

## II. THE MODEL

To obtain dynamics similar to those studied in molecular dynamics simulations of amorphous solids under oscillatory shear, we model the system as a point moving deterministically on a complex potential energy landscape where the coordinates of the particle are assumed to represent the vector of coordinates of all the particles in an amorphous solid:

$$\boldsymbol{r} = (x_1, y_1, z_1, x_2, y_2, z_3, \ldots, x_N, y_N, z_N). \tag{2}$$

The energy landscape is modeled as a random Gaussian field $\varphi(\boldsymbol{r})$ and the periodic shear is modeled as another random force field whose amplitude is oscillating in time with an angular frequency $\omega$ and amplitude $A$. The total force at a point $\boldsymbol{r}$ and time $t$ is of the form

$$\boldsymbol{F}(\boldsymbol{r}, t) = -\nabla\varphi(\boldsymbol{r}) + A\cos(\omega t)\,\boldsymbol{a}(\boldsymbol{r}), \tag{3}$$

where the first term is the gradient field stemming from the random potential and second term is the oscillatory forcing. In the second term $\boldsymbol{a}(\boldsymbol{r})$ is a random vector field independent of $\varphi$, representing the shear direction in the random energy landscape. The dynamics is assumed to be overdamped and time is discretized with equal time steps of length $\Delta t$. This gives rise to the discrete equation of motion:

$$\boldsymbol{r}_{n+1} = \boldsymbol{r}_n + \frac{\Delta t}{\gamma}\boldsymbol{F}(\boldsymbol{r}_n), \tag{4}$$

where $\gamma$ is a friction coefficient which we set to 1. For small-enough forcing frequencies $\omega$, the dynamics is approximately relaxational; if the force changes slowly, then the system stays close to a minimum which moves due to the forcing. When the minimum vanishes due to the forcing, the system flows to a new minimum (a fast process) and stays close to it until the new minimum vanishes as well. In this sense the dynamics is similar to the dynamics in quasistatic simulations of amorphous solids in which a force is applied slowly and the system stays close to the same minimum until it experiences a plastic event and moves to a different minimum. Here we chose to model the dynamics using the simplest form of a random field, a Guassian random field with zero mean. A Gaussian field $\boldsymbol{f}$ is a field whose value at each point is a random variable taken from the multivariate Gaussian distribution:

$$P(\boldsymbol{f}(\boldsymbol{r}_1), \boldsymbol{f}(\boldsymbol{r}_2), \ldots, \boldsymbol{f}(\boldsymbol{r}_N)) = \frac{1}{(2\pi)^{N/2}|\boldsymbol{\Sigma}|} e^{-\frac{1}{2}\sum_{i,j}\boldsymbol{f}(\boldsymbol{r}_i)\boldsymbol{\Sigma}^{-1}_{ij}\boldsymbol{f}(\boldsymbol{r}_j)}, \tag{5}$$

where

$$\boldsymbol{\Sigma}_{ij} = \langle \boldsymbol{f}(\boldsymbol{r}_i)\boldsymbol{f}(\boldsymbol{r}_j)\rangle = \boldsymbol{C}(\boldsymbol{r}_i, \boldsymbol{r}_j) \tag{6}$$

is the covariance matrix defined by the covariance function between the different spatial components of $\boldsymbol{r}_i$ and $\boldsymbol{r}_j$. By choosing different covariance functions we can change the properties of the random field.

To allow for simulations of systems in large space dimensions, we avoid creating the random field beforehand and randomly draw field realizations at new points in configuration space by keeping track of the previously visited points and imposing appropriate correlations between each new point and the previously visited points [41]. This enables us to extend our simulation to higher dimensions while minimizing computational complexity. At each time step we sample the values of $\nabla\varphi(\boldsymbol{r})$ and $\boldsymbol{a}(\boldsymbol{r})$, which are statistically independent random vectors with the dimensionality of the space, based on their values in the current position $\boldsymbol{r}_n$ and previous $n-1$ positions visited. We first discuss the calculation of the somewhat simpler field $\boldsymbol{a}(\boldsymbol{r})$. In order to account for the correlations, we use a conditional probability density function to draw the value of $\boldsymbol{a}(\boldsymbol{r})$ in the $(n+1)$th step [41]:

$$P\left(a^\alpha_{n+1}|a^\alpha_1, \ldots, a^\alpha_n\right) = \frac{P\left(a^\alpha_1, \ldots, a^\alpha_n, a^\alpha_{n+1}\right)}{P\left(a^\alpha_1, \ldots, a^\alpha_n\right)}, \tag{7}$$

where we denote $\boldsymbol{a}(\boldsymbol{r}_n) \equiv \boldsymbol{a}_n$ the force at step $n$, and the different components $a^\alpha(\boldsymbol{r})$ of $\boldsymbol{a}(\boldsymbol{r})$ are by assumption statistically independent. Since we are sampling a Gaussian field, the conditional probability distribution is a Gaussian whose expectation value $\boldsymbol{\mu}_{n+1}$, and variance $\sigma^2_{n+1}$ are obtained from Eq. (7) (see Appendix A). We used a Gaussian covariance function:

$$C(\rho) = e^{-\frac{1}{2}\rho^2}, \tag{8}$$

where $\rho = |\boldsymbol{r}_i - \boldsymbol{r}_j|$ and the correlation length was set to 1. In the case of the driving force direction $\boldsymbol{a}(\boldsymbol{r})$, the components in different Cartesian directions $a_\alpha(\boldsymbol{r})$ are assumed to be independent and thus the covariances are as follows:

$$\langle a_\alpha(\boldsymbol{r})a_\beta(\boldsymbol{r}+\boldsymbol{\rho})\rangle = \delta_{\alpha\beta}C(\boldsymbol{\rho}). \tag{9}$$

For the gradient field $\nabla\varphi(\boldsymbol{r})$, the different Cartesian components are correlated since they are derived from the same

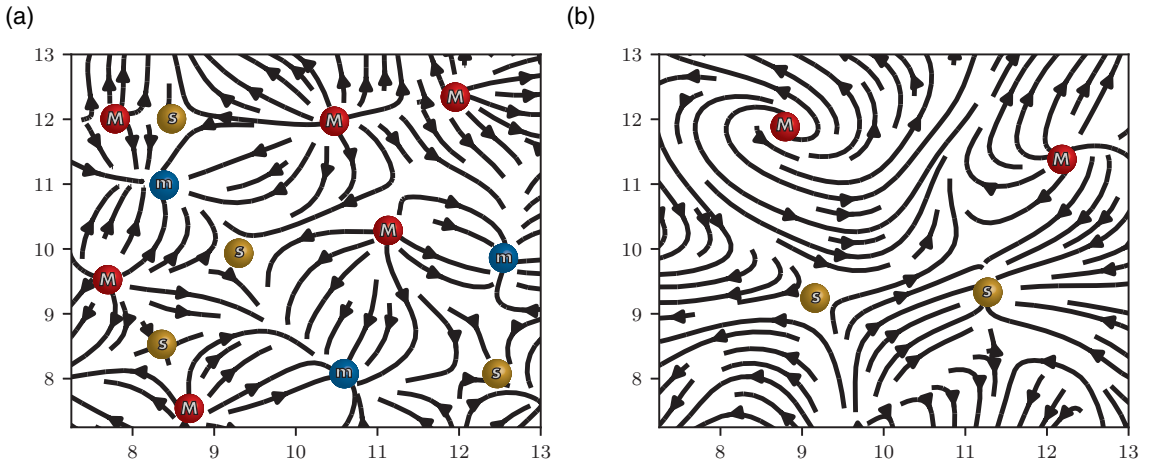


FIG. 1. Energy landscape sampling: A two-dimensional example of the force field generated by our simulation with driving force amplitude $A = 10$ at two different times: (a) at $A\cos(\omega t) = 0$ and (b) at $A\cos(\omega t) = 10$. We can see that the landscape generated contains a mixture of minima (blue) and maxima (red) surrounded by saddle points (yellow), where each minimum is surrounded by maxima and saddles which define its basin of attraction, and every saddle point connects separatrixes from which the system may evolve into two distinct minima. As time advances the landscape evolves smoothly in the first half period from (a) → (b) → (a) thus allowing the system to leave an initial minimum and explore other regions of state space by changing the stability of the minima.

potential $\varphi(\boldsymbol{r})$. This leads to the covariance function obtaining the form (see Appendix A for a detailed explanation):

$$\langle \nabla_\alpha \varphi(\boldsymbol{r}) \nabla_\beta \varphi(\boldsymbol{r}+\boldsymbol{\rho})\rangle = \frac{\partial^2 C(\rho)}{\partial \rho_\alpha \partial \rho_\beta} = (\delta_{\alpha\beta} - \rho_\alpha \rho_\beta) C(\rho), \tag{10}$$

and the probability distribution function for $\nabla_\alpha \varphi(\boldsymbol{r}_{n+1})$ is as follows:

$$P(\nabla_\alpha \varphi(\boldsymbol{r}_{n+1}) | \nabla_1 \varphi(\boldsymbol{r}_1), \nabla_1 \varphi(\boldsymbol{r}_2), \ldots, \nabla_d \varphi(\boldsymbol{r}_n)) = \frac{P(\nabla_1 \varphi(\boldsymbol{r}_1), \nabla_1 \varphi(\boldsymbol{r}_2), \ldots, \nabla_1 \varphi(\boldsymbol{r}_{n+1}), \nabla_2 \varphi(\boldsymbol{r}_1), \ldots, \nabla_d \varphi(\boldsymbol{r}_{n+1}))}{P(\nabla_1 \varphi(\boldsymbol{r}_1), \ldots, \nabla_d \varphi(\boldsymbol{r}_n))}. \tag{11}$$

To illustrate the dynamics induced by these fields, we show in Fig. 1 a representative realization of the field $\boldsymbol{F}(\boldsymbol{r})$ as a function of position for an amplitude $A = 10$ at two different times. In Fig. 1(a) we see the field $\boldsymbol{F}$ for $A\cos(\omega t) = 0$ which is $\boldsymbol{F}(\boldsymbol{r}) = -\nabla\varphi(\boldsymbol{r})$. Minima, maxima and saddle points are shown as blue, red, and yellow circles, respectively. In the absence of forcing, the system flows from any given initial position into one of the minima (the set of points leading to a minimum is its basin of attraction). Applying a nonzero forcing amplitude $A$ induces a periodic perturbation to the potential force field. In Fig. 1(b) we show how the force field looks at $A\cos(\omega t) = 10$. We can see that all the stable fixed points disappeared. This means that for this configuration, when the force reaches its maximum value, the system escapes the initial fixed point from which it started at $t = \pi/2\omega$ and can move to a different basin of attraction which leads to a different stable fixed point. This means that as the force oscillates, the particle explores other basins of the stationary configuration space, where a larger forcing amplitude enables the particle to explore more distant basins, and thus a larger portion of configuration space. If after a complete forcing cycle the particle returns to a previously visited basin, due to the deterministic nature of the dynamics (this comes from the fact that we do not "forget" previously visited sites and the correlations), then the system settles into a limit cycle in which it periodically revisits the same basins. In Fig. 2 we can see several trajectories on the same landscape with the same initial condition $(x_1, x_2) = (10, 10)$, where the state-space trajectory evolves differently for different driving-force amplitudes $A$. For $A = 3$ and $A = 6$ we see that the system is confined to a limit cycle around the origin; trajectories that correspond to larger forcing amplitudes $A$ explore larger and larger portions of space, and lead the system to settle into limit cycles further away from the origin. For $A = 15$ the system was able to explore even more distant parts of the state space and did not reach a limit cycle within the limited number of time steps used for this demonstration.

## III. RESULTS

We ran simulations in $d = 3$ and $d = 9$ with a random driving-force set to oscillate at an angular frequency $\omega = 1$ (low enough to allow for the formation of limit cycles) and a time step $\Delta t = 2\pi/70$ for different driving amplitudes $A$. In Fig. 3 we can see the typical behavior of the coordinates and the squared displacement $r^2(t)$ for $d = 9$ where we can see that the system experienced a random transient which approaches a limit cycle. This is the typical behavior observed in simulations of model amorphous solids [20–30,42]. We repeated the simulations for $d = 3$ with values of $A$ increasing from zero in increments of 0.4, where for each driving-force amplitude we used $n = 80$ independent realizations to obtain an ensemble average, and in each realization we ran the simulations up to 7000 steps or until the system reached a limit

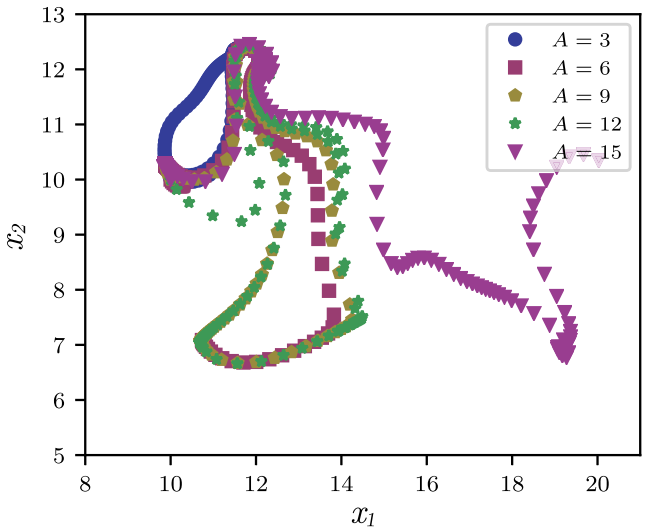


FIG. 2. Effect of increasing the forcing: Examples of state-space trajectories for five different simulations with different maximal forcing amplitudes $A$ on a two-dimensional landscape generated by our model, all starting from the same point $(x_1, x_2) = (10, 10)$ in state space. For $A = 3$ and $A = 6$ the system is confined to a limit cycle around the origin, whereas trajectories that correspond to larger forcing amplitudes explore larger and larger portions of space, and lead the system to settle into limit cycles further away from the origin. In this demonstration, for $A = 15$ the system was able to explore even more distant parts of the state space and did not reach a limit cycle.

cycle. To better understand the dynamics we evaluated $r^2(t)$ at zero forcing (after each driving-force period) and calculated the mean-squared displacement (MSD) $\langle r^2(t)\rangle$. We observe that for low-enough amplitudes the system always evolves into a limit cycle, in which the displacement is constant. However, for large-enough amplitudes we observe diffusive dynamics where $\langle r^2(t)\rangle \sim t$ [Fig. 4(a)]. Furthermore, the mean transient time $\tau$, the time required to reach a limit cycle, increases with the driving force amplitude and the increase is consistent with a power law divergence $|A - A_c|^{-\alpha}$ where in $d = 3$, $A_c = 26.0 \pm 0.4$ and $\alpha \approx 6.23$ [Fig. 4(c)]. The simulations were also repeated in $d = 9$ [Figs. 4(b) and 4(d)] with $A_c = 2.6 \pm 0.1$ and $\alpha \approx 3.6$, where we increased the maximum number of steps to 70,000 in order to obtain a more accurate characterization of the transition. As was mentioned above, the transition from periodic to diffusive behavior and the dependence of the critical amplitude on the system size are consistent with the phenomenology observed in simulations and experiments of cyclicly sheared amorphous solids [20–30].

Figures 5(a) and 5(d) illustrate how transients and limit cycles arise in a deterministic system with a rough energy landscape. In Fig. 5(a) we can see $r^2(t)$ of a trajectory ending in a limit cycle, and Fig. 5(d) shows its spatial trajectory (the simulation was performed in three dimensions). The latter shows that the system performed a random trajectory which entered a limit cycle once the trajectory intersected its own basin of attraction. Similarly to Fig. 2, the point at which self-intersection occurs is affected by the external forcing and larger forcing allows the system to explore larger regions of the configuration space which causes the system to travel further before the trajectory intersects its own basin of attraction which leads to longer transients. For large-enough forcing, it seems that the available state space is large enough that the probability to self-intersect becomes negligible and the system keeps diffusing forever. Another effect of the increase in available state space is that close to the critical point, the limit cycles can self-intersect after more than one forcing period. This has been observed in particle simulations, where it was shown that for forcing amplitudes close to the critical points, limit cycles can have periodicity which is a multiple of the periodicity of the external forcing [21,22,25]. Here we also observed this behavior, with two selected realizations shown in Fig. 5: In Figs 5(b) and 5(c) we can see limit cycles with periodicity $2T$ and $3T$, respectively. Both were obtained for a forcing amplitude $A = 7.6$ and space dimension $d = 3$. In Figs. 5(e) and 5(f) we can see the same limit cycles in three dimensions, where the parts of the trajectories that correspond to different forcing cycles are shown in different colors. This illustrates that the reason for a period larger than one is that the trajectory self intersects only after two or three forcing periods. In the next section we will compare these results to a molecular dynamics simulation of an amorphous solid under oscillatory shear.

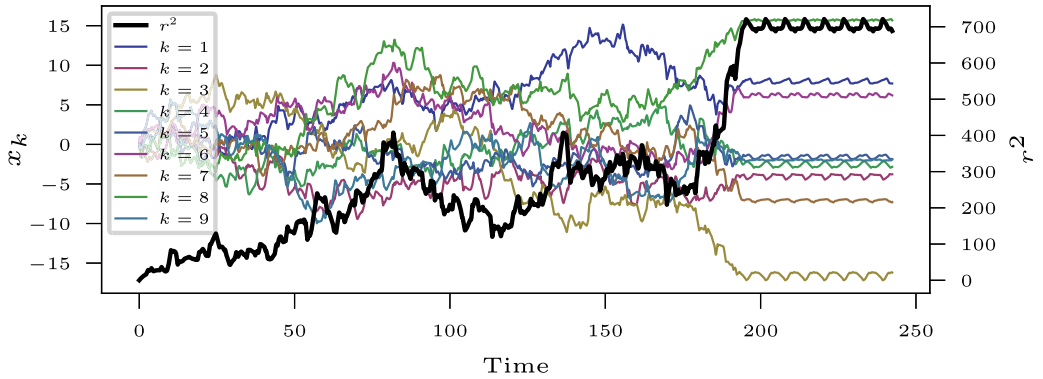


FIG. 3. Transient in many dimensions: Time evolution of $r^2(t)$ in nine dimensions (thick black line), and the position in each coordinate $x_k$, where $k = 1, \ldots, 9$ (thin lines). The coordinates initially exhibit random dynamics but end in a periodic state which is easily distinguishable from the random transient.

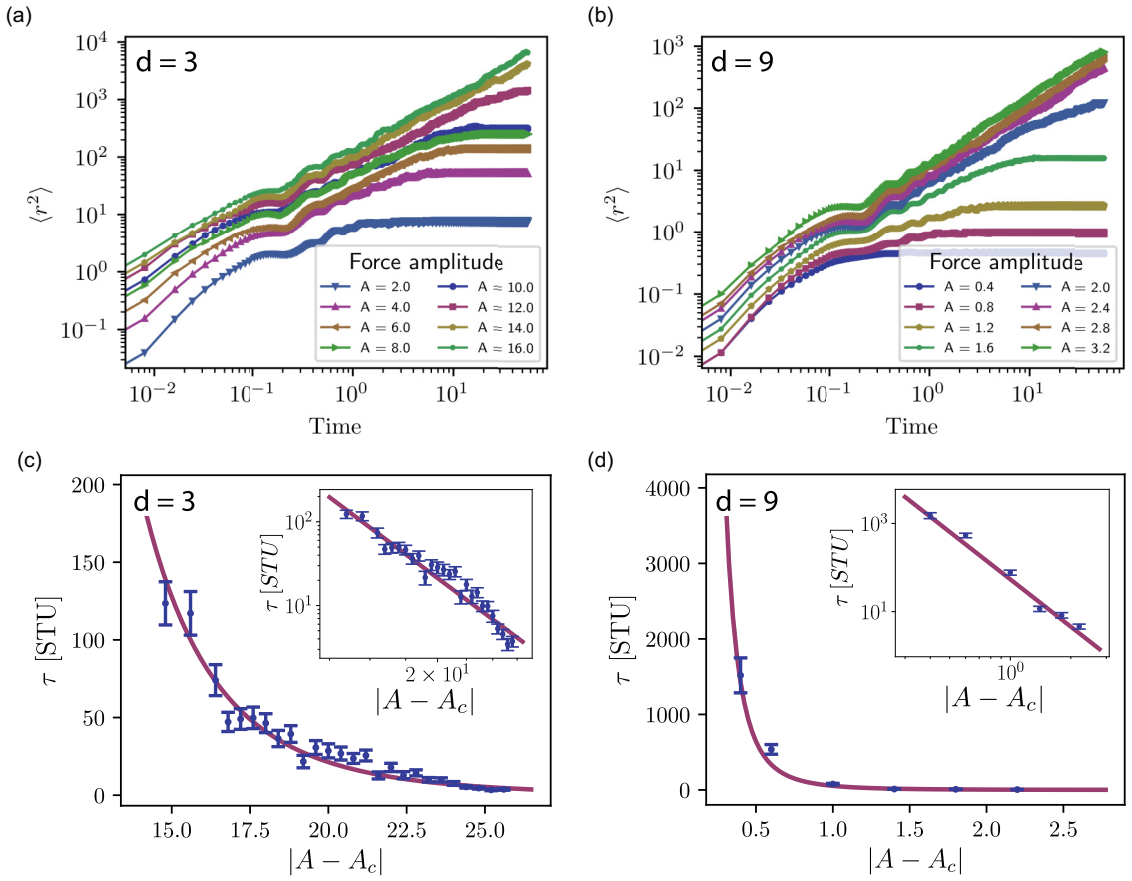


FIG. 4. Transition from periodic to diffusive dynamics: Time evolution of the mean squared displacement (MSD) sampled after each period of the driving force in (a) three dimensions averaged over 80 realizations and (b) nine dimensions averaged over 40 realizations for different driving-force amplitudes. Realizations under low driving-force amplitudes evolve into a limit cycle (visible as a flattening of the MSD), where the time it takes to reach a limit cycle is increased (visible by the growing length of the continuous lines) up to the point in which the system does not reach a limit cycle in the peak number of steps [equivalent to 630 simulation time units (STU)]. Mean transient time as a function of $|A - A_c|$ exhibiting power-law divergence (fitted curve) for $d = 3$ (c) and $d = 9$ (d). Insets: Same data in log-log scale.

## IV. COMPARISON TO MOLECULAR DYNAMICS SIMULATIONS

We further compare our results to two-dimensional molecular dynamics (MD) simulations of an amorphous solid prepared from a binary mixture and subjected to damped dynamics and oscillatory strain of the form:

$$\gamma = A \sin(\omega t). \tag{12}$$

where $\omega$ is the driving frequency. The simulations were kept at a very low temperature using a thermostat and the friction coefficient was large in order to minimize thermal effects. For further simulation details see Appendix C. To study the dynamics of the system as a function of the maximal shearing amplitude $A$, we follow the trajectory of one particle, which can be thought of as a projection of the vector of coordinates of the system into a two-dimensional plane. We observe that similarly to the landscape model, the particle and the system reach a limit cycle after a transient (Fig. 6). In Fig. 6(a) we can see the trajectories obtained for different amplitudes $A$. Initially, increasing $A$ does not change the dynamics significantly and the system reaches similar limit cycles. However, for large-enough $A$ the particle escapes into a different limit cycle that was not in the same region of state space as the one obtained previously. If we increase $A$ further, then the system still reaches a similar limit cycle but for a certain $A$ the limit cycle changes again. For significantly larger maximal strain amplitudes, the system reaches a limit cycle only after a long transient [Fig. 6(b)]. For the long transients, the system diffuses a distance larger than the particle diameter which precludes the possibility that the observed effects are due to caging. The similarities in the results lead us to suggest that a similar mechanism is responsible for the formation of limit cycles in both amorphous solids and the energy-landscape model.

## V. DISCUSSION

In this work we suggest a simple explanation for the phenomenology observed in the irreversibility transition in amorphous solids under oscillatory shear by studying the dynamics of a deterministic vector of coordinates exploring a random energy landscape. Specifically, we are interested in the appearance of limit cycles of different periodicities, in the transients leading to these limit cycles and in the transition from periodic to diffusive dynamics.

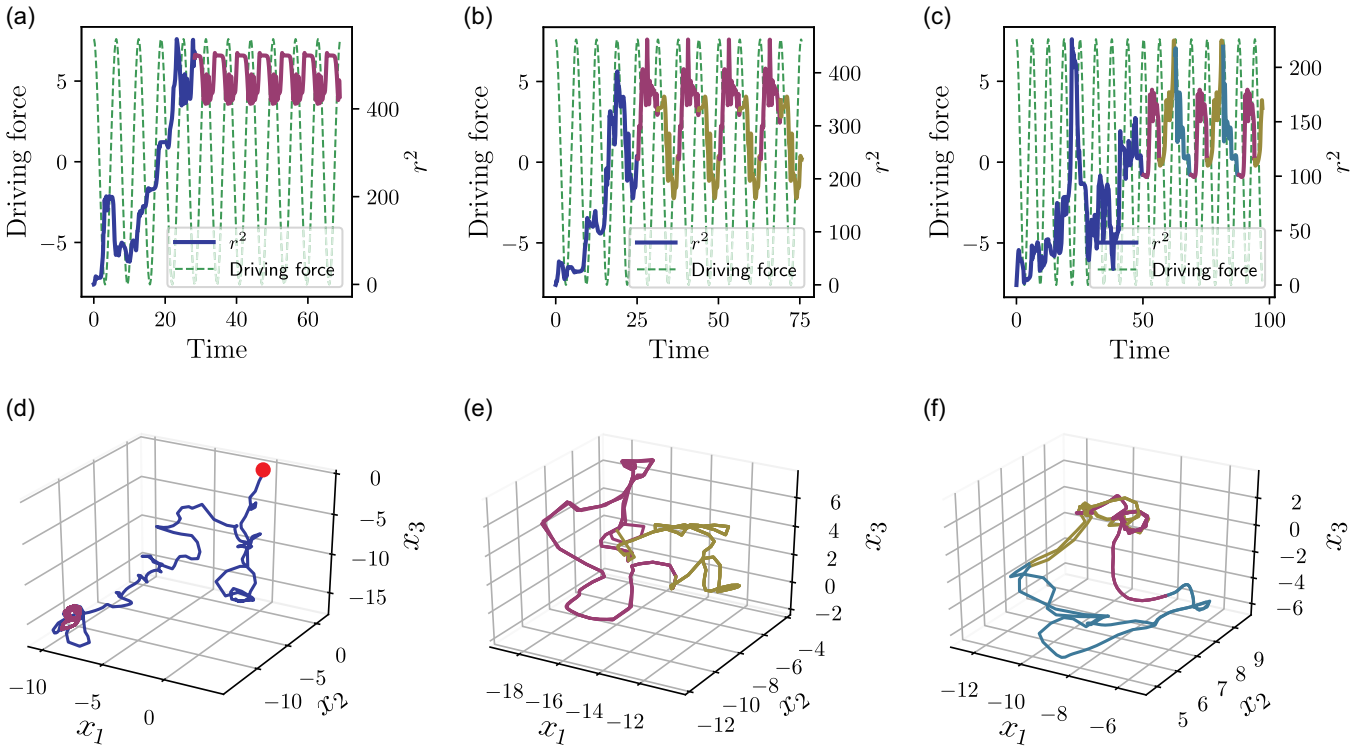


FIG. 5. Limit cycles and state-space trajectories: Several trajectories that evolved into limit cycles: [(a) and (d)] A trajectory forming a limit cycle of period $T$ (in maroon) after a transient (in blue), where (a) shows the $r^2(t)$ of the trajectory and (d) shows the three-dimensional trajectory (red dot represents the initial condition). [(b) and (e)] A trajectory reaching a limit cycle of period $2T$ where (b) shows $r^2(t)$ during the transient (blue) and the limit cycle (maroon and yellow) and (e) shows the three-dimensional trajectory during a cycle. The maroon part is the trajectory during the first forcing period, while the yellow part is the trajectory during the consecutive forcing period. Note that the trajectory self-intersects only after the second forcing period. [(c) and (f)] A limit cycle of period $3T$ where (c) shows $r^2(t)$ during the transient (blue) and the limit cycle (maroon, yellow and cyan) and (f) Shows the three-dimensional trajectory where each color represents a different forcing period. In all cases the driving force amplitude was $A = 7.6$ and the dimension was $d = 3$.

Since the dynamics is deterministic, once the basin of attraction of the trajectory self-intersects, the system enters a periodic trajectory. Here the differences between one-dimensional and multidimensional energy landscapes become important. Dynamics on a deterministic one-dimensional landscape is trivial and will always reach a fixed point. However, since our system is nonautonomous and periodically driven, it is equivalent to an autonomous system with a phase variable $\phi$ whose dynamics is described by an equation of motion $\dot{\phi} = \omega$, where $\phi$ is defined modulo $2\pi$. For a one-dimensional system the dynamics is thus confined to an infinite cylinder since the spatial coordinate is unbounded but

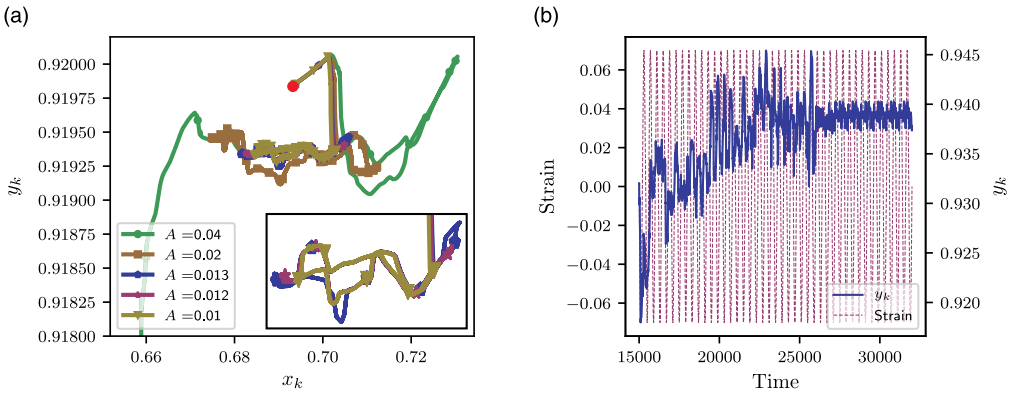


FIG. 6. Molecular dynamics simulations: (a) Change in the state-space trajectories of one particle following a gradual increase in the maximal strain amplitude. Here $x_k$ and $y_k$ are the coordinates (normalized by the system size $L$) of the $k = 500$ particle out of $N = 1024$. (b) $y$ coordinate of one of the particles in a MD simulation subjected to oscillatory shear with $A = 0.07$, $\omega = 0.0157$. The coordinate shows transient random dynamics and the settling into a limit cycle with a periodicity $2T$ (red dot represents the initial condition).

the phase coordinate is compact. In this case, assuming that the dynamics in the $x$ coordinate is random but unbiased it will always self-intersect and form a period-one limit cycle.

However, for $d = 3$ and $d = 9$, we have shown that a simple energy landscape model with Gaussian statistics can reproduce many of the distinct behaviors observed in amorphous solids such as limit cycles of different periodicities and a transition from asymptotically periodic to asymptotically diffusive dynamics. The model provides an appealing explanation for the observation of limit cycles with periods $nT$ , $n \in \mathbb{N}$—when the forcing is small, the vector of coordinates is limited to a small part of the energy landscape and the trajectory self-intersects after a short transient and forms a limit cycle. However, when the amplitude of the forcing increases, the volume explored by the vector of coordinates (here we think of it as a point in state space) increases and it takes a longer time for its trajectory to self-intersect. This idea is supported by the similarity of Figs. 2 and 3, which show the results of our model, to the results of the molecular dynamics simulations shown in Fig. 6(a) which provides a strong indication that this is indeed the mechanism also in the amorphous solid, even though the amorphous solid has a much more complex energy landscape. This notion can also explain why cycles with periodicities $n > 1$ occur: When the accessible volume is large but bounded, and the space dimension is larger than 1, the trajectory may cross itself after more than one cycle as is seen in Figs. 5(b) and 5(c) for $d = 3$. The appearance of a transition from asymptotically periodic to unbounded, diffusive dynamics (Fig. 4) which involves a diverging timescale with a power-law divergence, together with the appearance of periods larger than 1 (Fig. 5), which are also observed in MD simulations [21,25,26], hint that these aspects of the irreversibility transition in amorphous solids can be explained in terms of a forced, deterministic, dynamics on a random energy landscape.

The observation that many aspects of the dynamics are captured by a model of dynamics on a random energy landscape with Gaussian statistics is encouraging since the results obtained in three dimensions are qualitatively similar to the results obtained in higher dimensions, which may help visualize and obtain a deeper understanding of the relevant features of energy landscapes which are responsible to the irreversibility transition. Furthermore, the fact that the transition can be reproduced, at least qualitatively, on a Gaussian surface is encouraging since analytical calculations are much more tractable on an energy landscape with Gaussian statistics than on other, more complex landscapes. Specifically, that the geometrical phase transition studied analytically in Gaussian surfaces subjected to forcing [9,15] may be related to the transition from having many limit cycles to an unbounded diffusive dynamics observed here.


## ACKNOWLEDGMENTS

I.R. and A.S. were supported by the Israel Science Foundation through Grant No. 1301/17. O.G. acknowledges insightful discussions with Oded Agam.


## APPENDIX A: ALGORITHM DETAILS

In our algorithm we assume that the Gaussian fields $\varphi(\boldsymbol{r})$ and $\boldsymbol{a}(\boldsymbol{r})$ are normalized and centered around zero:

$$\langle a_\alpha(r)\rangle = \langle \varphi(\boldsymbol{r})\rangle = 0, \tag{A1}$$

and the covariance function is chosen to be a Gaussian of the form:

$$\langle a_\alpha(\boldsymbol{r}_i)a_\beta(\boldsymbol{r}_j)\rangle \equiv C_{\alpha\beta}(\boldsymbol{r}_i,\boldsymbol{r}_j) = \delta_{\alpha\beta}\, e^{-\frac{1}{2}|\boldsymbol{r}_i-\boldsymbol{r}_j|^2}, \tag{A2}$$

$$\langle \varphi(\boldsymbol{r}_i)\varphi(\boldsymbol{r}_j)\rangle \equiv C(\boldsymbol{r}_i,\boldsymbol{r}_j) = e^{-\frac{1}{2}|\boldsymbol{r}_i-\boldsymbol{r}_j|^2}, \tag{A3}$$

where $\alpha = 1,\ldots,d$ is an index of the different Cartesian components.

### 1. The forcing field: $\boldsymbol{a}(\boldsymbol{r})$

In order to sample the force at point $\boldsymbol{r}_{n+1}$ visited at the $(n+1)$th step when the forces at the previous $n$ steps were already determined, we calculate the conditional probability distribution given by Eq. (7). Since the forces at all the previous steps were already determined, the denominator is already known. We therefore calculate the numerator given by the probability density function:

$$P\left(a_1^\alpha,\ldots,a_{n+1}^\alpha\right) = \frac{e^{-\frac{1}{2}\sum_{i,j} a_i^\alpha \left[\boldsymbol{\Sigma}(n+1)\right]^{-1}_{ij} a_j^\alpha}}{\sqrt{(2\pi)^{(n+1)}|\boldsymbol{\Sigma}(n+1)|}}. \tag{A4}$$

Here and in the following, $a_i^\alpha \equiv a_\alpha(\mathbf{r}_i)$. In the following, we will also drop the index $\alpha$ for convenience and will relate to $a$ as a scalar which is one of the Cartesian components of $\boldsymbol{a}$. Note also that while $a_n$ is the value of $a$ in the $n$th time step, $\boldsymbol{a}(n)$ is a vector whose elements are all the sites visited up to step $n$: $\boldsymbol{a}(n) = (a_1, a_2, \ldots, a_n)$. The matrix $\boldsymbol{\Sigma}(n+1)$ is the covariance matrix after $n+1$ steps which can be written in the form:

$$\boldsymbol{\Sigma}(n+1) = \begin{bmatrix} \boldsymbol{\Sigma}(n) & \boldsymbol{b}(n) \\ \boldsymbol{b}^T(n) & c \end{bmatrix}, \tag{A5}$$

where the matrix $\boldsymbol{\Sigma}(n)$ is the $(n\times n)$ covariance matrix after $n$ steps, $\boldsymbol{b}(n)$ is an $n$-vector defined by the covariance between the point $\boldsymbol{r}_{n+1}$ and all the previously visited points ($\boldsymbol{r}_i$, $i = 1, 2, \ldots, n$), or $b_i(n) = C(\boldsymbol{r}_i, \boldsymbol{r}_{n+1})$, and $c = C(\boldsymbol{r}_{n+1}, \boldsymbol{r}_{n+1}) \equiv 1$. $\boldsymbol{\Sigma}(n+1)$ can be inverted blockwise [43] to find $\boldsymbol{\Sigma}^{-1}(n+1)$ in terms of the $n$-step matrices and vectors:

$$\boldsymbol{\Sigma}^{-1}(n+1) = \begin{bmatrix} \boldsymbol{\Sigma}^{-1}(n) + \boldsymbol{\Sigma}^{-1}(n)\boldsymbol{b}(n)s^{-1}(n)\boldsymbol{b}^T(n)\boldsymbol{\Sigma}^{-1}(n) & -\boldsymbol{\Sigma}^{-1}(n)\boldsymbol{b}(n)s^{-1}(n) \\ -s^{-1}(n)\boldsymbol{b}^T(n)\boldsymbol{\Sigma}^{-1}(n) & s^{-1}(n) \end{bmatrix}, \tag{A6}$$

here $s(n)$ is as follows:

$$s(n) \equiv c - \boldsymbol{b}^T(n)\boldsymbol{\Sigma}^{-1}(n)\boldsymbol{b}(n). \tag{A7}$$

Since $\boldsymbol{\Sigma}(n)$ and $\boldsymbol{b}(n)$ are known we can use Eq. (A6) to calculate $\boldsymbol{\Sigma}^{-1}(n+1)$ and find both numerator and denominator of Eq. (7). To extract from it a probability distribution for $a_{n+1}$ we complete the square inside the exponent in Eq. (A4):

$$\boldsymbol{a}^T(n+1)\boldsymbol{\Sigma}^{-1}(n+1)\boldsymbol{a}(n+1) = \left\{a_{n+1} - \boldsymbol{a}^T(n)\boldsymbol{\Sigma}^{-1}(n)\boldsymbol{b}(n)\right\}s^{-1}(n)\left\{a_{n+1} - \boldsymbol{b}^T(n)\boldsymbol{\Sigma}^{-1}(n)\boldsymbol{a}(n)\right\} + \boldsymbol{a}^T(n)\boldsymbol{\Sigma}^{-1}(n)\boldsymbol{a}(n)$$

the numerator is now a product of two terms of the form:

$$e^{-\frac{\left(a^\alpha_{n+1}-\mu^\alpha_{n+1}\right)^2}{2\sigma^2_{n+1}}}\, e^{-\boldsymbol{a}^T(n)\boldsymbol{\Sigma}^{-1}(n)\boldsymbol{a}(n)}, \tag{A8}$$

where $\mu_{n+1}$ and $\sigma^2_{n+1}$ are as follows:

$$\mu_{n+1} = \boldsymbol{a}^T(n)\boldsymbol{\Sigma}^{-1}(n)\boldsymbol{b}(n) \tag{A9}$$

and

$$\sigma^2_{n+1} = c - \boldsymbol{b}^T(n)\boldsymbol{\Sigma}^{-1}(n)\boldsymbol{b}(n). \tag{A10}$$

However, the second exponential cancels with the denominator and we get that the probability distribution function for the force component $a^\alpha$ in the $(n+1)$th step is as follows:

$$P\left(a^\alpha_{n+1}|a^\alpha_1,\ldots,a^\alpha_n\right) = \frac{1}{\sqrt{2\pi}\sigma_{n+1}} e^{-\left(\frac{a^\alpha_{n+1}-\mu^\alpha_{n+1}}{\sqrt{2}\sigma_{n+1}}\right)^2}, \tag{A11}$$

which we use to find the value of $a^\alpha_{n+1}$ and calculate the position at the $(n+1)$th time step.

### 2. The gradient field: $\nabla\varphi(\boldsymbol{r})$

In our algorithm we do not evaluate the potential field directly but rather the conservative force field $\nabla\varphi(\boldsymbol{r})$. For a gradient field, the different components of the vector are not statistically independent and thus the covariance function is modified to take this into account. We first note that:

$$\Sigma_{\alpha\beta} = \langle\nabla_\alpha\varphi(\boldsymbol{r})\nabla_\beta\varphi(\boldsymbol{r}+\boldsymbol{\rho})\rangle = \frac{\partial^2 C(\boldsymbol{\rho})}{\partial\rho_\alpha\partial\rho_\beta}, \tag{A12}$$

substituting a Gaussian covariance function, this leads to the following:

$$\langle\nabla_\alpha\varphi(\boldsymbol{r})\nabla_\beta\varphi(\boldsymbol{r}+\boldsymbol{\rho})\rangle = (\delta_{\alpha\beta} - \rho_\alpha\rho_\beta)C(\boldsymbol{\rho}). \tag{A13}$$

Therefore, the covariance for the gradient term mixes the different spatial components of the force which leads to appropriate alterations of Eq. (A6), Eq. (A9), and Eq. (A10) which are then used to find the mean and variance for the gradient field from the probability distribution, Eq. (11).

## APPENDIX B: NUMERICAL LIMITATIONS AND APPROXIMATIONS

A potential problem in our algorithm is that the covariance matrix $\boldsymbol{\Sigma}$ becomes numerically ill-conditioned when two previously visited points are close-by. To overcome this difficulty we use a singular-value decomposition (SVD) for calculating the inverse of the covariance matrix. When $\boldsymbol{\Sigma}$ is invertible, the SVD method gives the exact inverse. When the matrix becomes ill conditioned, we set a lower cut-off value for the small singular values and when they fall below it (e.g., $10^{-6}$ in our simulation) we set the corresponding singular values of $\boldsymbol{\Sigma}^{-1}$ to zero. We want to emphasize that this approximation is required due to limitations of the numerics (the problem of calculating eigenvalues for a matrix with a large condition number) and that the singularity of $\boldsymbol{\Sigma}^{-1}$ should not affect the analytical calculation as we will show below for a simple one-dimensional example.

In the following we analytically estimate the deviation between the analytical and numerical solution that uses the aforementioned procedure for a simple geometry. To simplify the calculation, we choose only three points from a hypothetical trajectory (Fig. 7). First consider two adjacent points at distance $\epsilon \ll 1$ apart (points 1 and 2 in Fig. 7) and assume that they were previously visited. The covariance matrix for these two points will be ill conditioned and will be written as:

$$\boldsymbol{\Sigma} = \begin{bmatrix} 1 & f(\epsilon) \\ f(\epsilon) & 1 \end{bmatrix} \approx \begin{bmatrix} 1 & 1+\frac{\epsilon^2}{2}f''(0) \\ 1+\frac{\epsilon^2}{2}f''(0) & 1 \end{bmatrix}, \tag{B1}$$

where $f''(0) = 1$ for the covariance function that we chose. In order to evaluate the force at a third point at distance $\ell$ from the first two points (point 3 in Fig. 7) we need the covariance vector $\boldsymbol{b}$ for the third point which will take the form:

$$\boldsymbol{b} = \begin{bmatrix} f(\ell) \\ f(\ell+\epsilon) \end{bmatrix} \approx \begin{bmatrix} f(\ell) \\ f(\ell) + f'(\ell)\epsilon \end{bmatrix}. \tag{B2}$$

The inverse of $\boldsymbol{\Sigma}$ is then calculated analytically:

$$\boldsymbol{\Sigma}^{-1} = \begin{bmatrix} -\frac{4}{4\epsilon^2+\epsilon^4} & \frac{4+2\epsilon^2}{4\epsilon^2+\epsilon^4} \\ \frac{4+2\epsilon^2}{4\epsilon^2+\epsilon^4} & -\frac{4}{4\epsilon^2+\epsilon^4} \end{bmatrix}. \tag{B3}$$

We need to make sure that the result is not divergent in the conditions of a limit cycle in which $\epsilon \to 0$. Starting with calculating $\sigma$ [Eq. (A10)], we need to calculate $\boldsymbol{b}^T\boldsymbol{\Sigma}^{-1}\boldsymbol{b}$, and in the limit of $\epsilon \to 0$ we get

$$\lim_{\epsilon\to 0}\left\{\boldsymbol{b}^T\boldsymbol{\Sigma}^{-1}\boldsymbol{b}\right\} = f(\ell)^2 - f'(\ell)^2, \tag{B4}$$

which is not divergent. We can treat $\mu$ in a similar way [Eq. (A9)]. Since the force at each point is determined by $\mu$

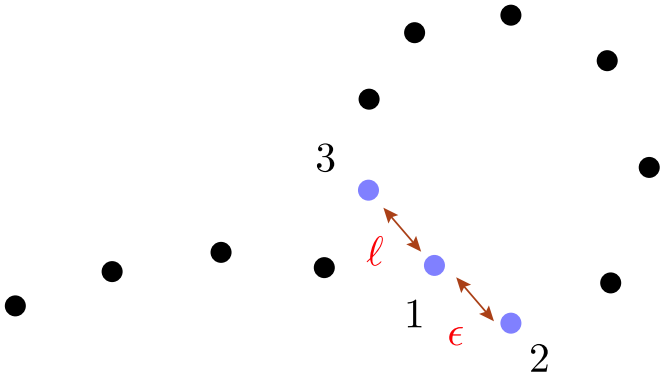


FIG. 7. A cartoon illustrating a trajectory and the three points on it used in the definitions in the analytical derivation of Eq. (B1) and Eq. (B2).

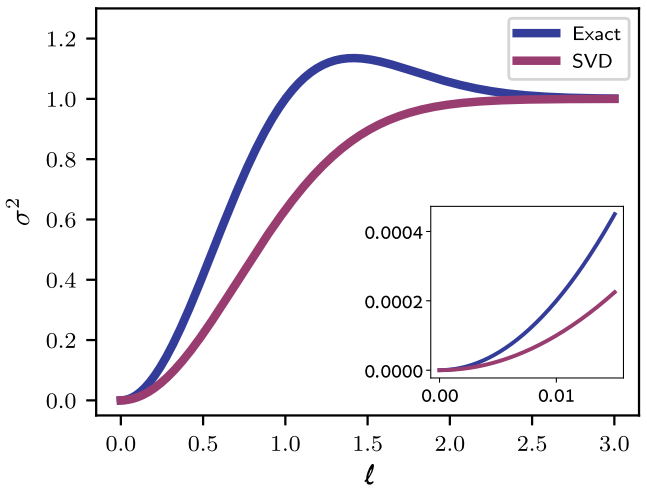


FIG. 8. A comparison between the exact and approximate calculation of $\sigma^2$ [Eq. (A10)] in the limit of $\epsilon \to 0$, the exact analytical calculation obtained by Eq. (B4) (blue) and the SVD solution obtained by Eq. (B9) (magenta). The inset is an enlargement of the region of small $\ell$ relevant to the case of a limit cycle.

and $\sigma$ alone, and since $\sigma \to 0$ as $\epsilon \to 0$ (and thus $\boldsymbol{a}_2 \to \boldsymbol{a}_1$ as $\epsilon \to 0$), we can expand $\boldsymbol{a}_2$ to the first order of $\epsilon$ and get

$$\boldsymbol{a} = \begin{bmatrix} \boldsymbol{a}_1 \\ \boldsymbol{a}_2 \end{bmatrix} \approx \begin{bmatrix} \boldsymbol{a}_1 \\ \boldsymbol{a}_1 + \boldsymbol{a}_1' \epsilon \end{bmatrix}, \tag{B5}$$

thus $\mu$ is also nondivergent in the limit of $\epsilon \to 0$.

To test the accuracy of our simulation we employ the SVD method on $\Sigma$ given by Eq. (B1). Since $\Sigma$ is symmetric, it can be decomposed as $\Sigma = PDP^T$, where $D$ is a diagonal matrix containing the singular values of $\Sigma$. We get

$$D_{\mathrm{SVD}}^{-1} = \begin{bmatrix} \frac{2}{\epsilon^2} & 0 \\ 0 & \frac{2}{4+\epsilon^2} \end{bmatrix}, \tag{B6}$$

meaning that in our simulation for $\epsilon < 7 \times 10^{-4}$ we will get

$$D_{\mathrm{SVD}}^{-1} = \begin{bmatrix} 0 & 0 \\ 0 & \frac{2}{4+\epsilon^2} \end{bmatrix}, \tag{B7}$$

and therefore

$$\Sigma_{\mathrm{SVD}}^{-1} = \begin{bmatrix} \frac{1}{4+\epsilon^2} & \frac{1}{4+\epsilon^2} \\ \frac{1}{4+\epsilon^2} & \frac{1}{4+\epsilon^2} \end{bmatrix}, \tag{B8}$$

and in the limit of $\epsilon \to 0$ we get

$$\lim_{\epsilon \to 0} \left\{ \boldsymbol{b}^T \boldsymbol{\Sigma}_{\mathrm{SVD}}^{-1} \boldsymbol{b} \right\} = f(\ell)^2, \tag{B9}$$

which deviates from the result of the analytic calculation [Eq. (B4)] by $f'(\ell)^2$. We have tested the validity of our algorithm under the expected conditions when the time steps are very small or $\epsilon \to 0$, and showed that there is no singularity in either $\mu$ or $\sigma$, thus making our calculation mathematically valid. However, the effects of our numerical approximations are manifested in a deviation from the analytic solution. In Fig. 8 we see how $\sigma^2$ is affected by our approximations, where in the inset we can see that for small values of $\ell$ the differences are small. Since in a real setup, which contains hundreds of points, the covariances decrease exponentially with the distance, we expect $\ell$ to be either small or dominated by the covariances with closer points (assuming that the time steps are small enough). In both cases, we regard the inaccuracy due to the approximation as a numerical noise.

## APPENDIX C: MOLECULAR DYNAMICS SIMULATIONS

We simulated $N$ soft disks [44] which were chosen to be a 50:50 binary mixture of small and large particles where the large particles were 1.4 the size of the small particles. Using a binary mixture in MD simulations is a necessity in order to avoid crystallization, and a 1:1.4 ratio between small and large particles is used to impose geometrical frustration, i.e., this ratio does not allow for a formation of a crystal lattice [45,46]. This setup is widely used in experiments and industrial applications when preparing bulk-metallic glass alloys [47,48]. The soft-disk interaction potential was chosen to be harmonic:

$$u_{ij}(r_{ij}) = \begin{cases} \frac{1}{2}k(a_i + a_j - r_{ij})^2, & r_{ij} \leqslant a_i + a_j \\ 0, & r_{ij} > a_i + a_j \end{cases},$$

where $a_i = 1$ or 1.4 is the particle radius. We used damped dynamics with an oscillatory drive:

$$m_i \frac{dv_x^i}{dt} = -\frac{\partial U}{\partial x_i} - 2\pi f A \cos(2\pi f t) - \eta v_x^i, \tag{C1}$$

$$m_i \frac{dv_y^i}{dt} = -\frac{\partial U}{\partial y_i} - \eta v_y^i, \tag{C2}$$

$$x^i = \frac{dv_x^i}{dt} + A \sin(2\pi f t), \tag{C3}$$

$$y^i = \frac{dv_y^i}{dt}, \tag{C4}$$

which were coupled with the Lees-Edwards boundary conditions [49]. The parameters $m_i$, $k$, $\eta$, and $f$ were fixed $m_i = 1$, $k = 300$, $\eta = 1$, and $f = 0.0025$ (in Lennard-Jones units) whereas the drive amplitude $A$ was used as a varying control parameter. The equations of motion were solved using the leap-frog algorithm and the dynamics was thermostated using the Berendsen thermostat [50].

[1] P. G. Debenedetti and F. H. Stillinger, Nature **410**, 259 (2001).
[2] A. Cavagna, Phys. Rep. **476**, 51 (2009).
[3] M. Goldstein, J. Chem. Phys. **51**, 3728 (1969).
[4] T. S. Grigera, A. Cavagna, I. Giardina, and G. Parisi, Phys. Rev. Lett. **88**, 055502 (2002).
[5] B. Doliwa and A. Heuer, Phys. Rev. E **67**, 030501(R) (2003).
[6] B. Doliwa and A. Heuer, Phys. Rev. Lett. **91**, 235501 (2003).
[7] A. Heuer, J. Phys.: Condens. Matter **20**, 373101 (2008).
[8] A. J. Bray and D. S. Dean, Phys. Rev. Lett. **98**, 150201 (2007).

[9] Y. V. Fyodorov and C. Nadal, Phys. Rev. Lett. **109**, 167203 (2012).
[10] Y. V. Fyodorov, Phys. Rev. Lett. **92**, 240601 (2004).
[11] V. Ros, G. Ben Arous, G. Biroli, and C. Cammarota, Phys. Rev. X **9**, 011003 (2019).
[12] S. Becker, Y. Zhang, and A. A. Lee, Phys. Rev. Lett. **124**, 108301 (2020).
[13] Y. V. Fyodorov and P. Le Doussal, Phys. Rev. E **101**, 020101(R) (2020).
[14] Y. V. Fyodorov, P. Le Doussal, A. Rosso, and C. Texier, Ann. Phys. **397**, 1 (2018).
[15] J. Ipsen and P. Forrester, J. Phys. A: Math. Theore. **51**, 474003 (2018).
[16] M. J. Osborne and D. J. Lacks, J. Phys. Chem. B **108**, 19619 (2004).
[17] M. E. Cates, J. P. Wittmer, J.-P. Bouchaud, and P. Claudin, Phys. Rev. Lett. **81**, 1841 (1998).
[18] P. Sollich, Phys. Rev. E **58**, 738 (1998).
[19] J. R. Royer and P. M. Chaikin, Proc. Natl. Acad. Sci. U.S.A. **112**, 49 (2015).
[20] S. Slotterback, M. Mailman, K. Ronaszegi, M. van Hecke, M. Girvan, and W. Losert, Phys. Rev. E **85**, 021309 (2012).
[21] I. Regev, T. Lookman, and C. Reichhardt, Phys. Rev. E **88**, 062401 (2013).
[22] I. Regev, J. Weber, C. Reichhardt, K. A. Dahmen, and T. Lookman, Nat. Commun. **6**, 8805 (2015).
[23] N. C. Keim and P. E. Arratia, Soft Matter **9**, 6222 (2013).
[24] K. Hima Nagamanasa, S. Gokhale, A. K. Sood, and R. Ganapathy, Phys. Rev. E **89**, 062308 (2014).
[25] T. Kawasaki and L. Berthier, Phys. Rev. E **94**, 022615 (2016).
[26] D. Fiocco, G. Foffi, and S. Sastry, Phys. Rev. E **88**, 020301(R) (2013).
[27] N. V. Priezjev, Phys. Rev. E **93**, 013001 (2016).
[28] J. C. Pfeifer, T. Bischoff, G. Ehlers, and B. Eckhardt, Phys. Rev. E **92**, 062208 (2015).
[29] P. Leishangthem, A. D. Parmar, and S. Sastry, Nat. Commun. **8**, 14653 (2017).
[30] N. V. Priezjev, Phys. Rev. E **95**, 023002 (2017).
[31] I. Regev, C. Reichhardt, and C. J. O. Reichhardt, Modell. Simul. Mater. Sci. Eng. **27**, 084004 (2019).
[32] K. Nagasawa, K. Miyazaki, and T. Kawasaki, Soft Matter **15**, 7557 (2019).
[33] M. Mungan, S. Sastry, K. Dahmen, and I. Regev, Phys. Rev. Lett. **123**, 178002 (2019).
[34] L. Corté, P. Chaikin, J. Gollub, and D. Pine, Nat. Phys. **4**, 420 (2008).
[35] D. Fiocco, G. Foffi, and S. Sastry, J. Phys.: Condens. Matter **27**, 194130 (2015).
[36] X. Ni, H. Zhang, D. B. Liarte, L. W. McFaul, K. A. Dahmen, J. P. Sethna, and J. R. Greer, Phys. Rev. Lett. **123**, 035501 (2019).
[37] B. L. Brown, C. Reichhardt, and C. Reichhardt, New J. Phys. **21**, 013001 (2019).
[38] I. Regev and T. Lookman, J. Phys.: Condens. Matter **31**, 045101 (2018).
[39] E. Schinasi-Lemberg and I. Regev, Phys. Rev. E **101**, 012603 (2020).
[40] Y. Jin and H. Yoshino, Nat. Commun. **8**, 14935 (2017).
[41] A. Pines, M.Sc. thesis, The Hebrew University of Jerusalem, 2010.
[42] S. Mukherji, N. Kandula, A. K. Sood, and R. Ganapathy, Phys. Rev. Lett. **122**, 158001 (2019).
[43] S. Banerjee and A. Roy, *Linear Algebra and Matrix Analysis for Statistics* (CRC Press, Boca Raton, 2014), 1st ed.
[44] M. M. Hurley and P. Harrowell, Phys. Rev. E **52**, 1694 (1995).
[45] H. Tanaka, T. Kawasaki, H. Shintani, and K. Watanabe, Nat. Mater. **9**, 324 (2010).
[46] T. Kawasaki, T. Araki, and H. Tanaka, Phys. Rev. Lett. **99**, 215701 (2007).
[47] L. Berthier and G. Biroli, Rev. Mod. Phys. **83**, 587 (2011).
[48] Z. Raza, B. Alling, and I. A. Abrikosov, J. Phys.: Condens. Matter **27**, 293201 (2015).
[49] A. Lees and S. Edwards, J. Phys. C: Solid State Phys. **5**, 1921 (1972).
[50] M. P. Allen and D. J. Tildesley, *Computer Simulation of Liquids* (Oxford University Press, Oxford, 1989).